Journal of Alloys and Compounds 651 (2015) 24–28

Contents lists available at ScienceDirect

Journal of Alloys and Compounds

journal homepage: http://www.elsevier.com/locate/jalcom

# Mesoporous $NiCo_2O_4$ nanosheets with enhance sodium ion storage properties

Kaiqiang Zhou [a], Zhensheng Hong [a, *], Chaobing Xie [a], Hong Dai [b], Zhigao Huang [a, **]

[a] Fujian Provincial Key Laboratory of Quantum Manipulation and New Energy Materials, College of Physics and Energy, Fujian Normal University, Fuzhou, Fujian 350108, PR China
[b] College of Chemistry and Chemical Engineering, Fujian Normal University, Fujian, Fuzhou 350108, PR China

ARTICLE INFO

*Article history:*
Received 3 July 2015
Received in revised form
8 August 2015
Accepted 17 August 2015
Available online 20 August 2015

*Keywords:*
$NiCo_2O_4$
Nanosheets
Mesoporous
Sodium ion batteries

ABSTRACT

Two kinds of the $NiCo_2O_4$ nanosheets constructed by interconnected nanoparticles with different microstructures, including ultrathin $NiCo_2O_4$ nanosheets ($NiCo_2O_4$-UNSs) and common $NiCo_2O_4$ nanosheets ($NiCo_2O_4$-NSs), were controllably synthesized by a facile method. The structure and morphology of the $NiCo_2O_4$ nanosheets were analyzed and characterized by XRD, SEM and TEM. $NiCo_2O_4$-UNSs possess a large surface area (119 $m^2\ g^{-1}$) and narrow pore distribution (around 5 nm). Subsequently, the Na-ion storage properties of such $NiCo_2O_4$ nanosheets were investigated by sodium half-cells. The ultrathin $NiCo_2O_4$ nanosheets ($NiCo_2O_4$-NSs) exhibit much improved performance than that of $NiCo_2O_4$-NSs with a high reversible capacity of 690.4 mA h $g^{-1}$ at 100 $mAg^{-1}$ and 141.8 mA h $g^{-1}$ at the current density of 1000 mA $g^{-1}$ in the voltage window of 0.01–2.5 V. Furthermore, a reversible capacity of about 203.7 mA h $g^{-1}$ can be remained after 50 cycles at 200 $mAg^{-1}$.

© 2015 Published by Elsevier B.V.

## 1. Introduction

Taking into account the consumption of the fossil fuels and the pollution of the greenhouse gas emissions, it has created a demand to seek the new energy storage systems and renewable energy resources, such as solar power, water power and so on. Lithium ion batteries (LIBs) have been considered as the next generational energy storage and conversion devices with high energy and power density [1,2]. LIBs have been widely used in the electronics industry in the past two decades. However, with the development of the electronics industry, the demand of the lithium ion batteries has been significantly increasing. Although LIBs have an excellent cycling performance and high energy density, there is an increasing concern about the cost and the abundance of the lithium reserves [3,4]. Therefore, many of scientists have already made great efforts to explore a new energy storage device.

In view of the natural abundance and the electrode potential of sodium resources, Na-ion batteries (NIBs) were considered as a promising battery system to replace Li-ion battery [5–7]. The concept of sodium ion batteries was first proposed by Doeff et al. [8]. However, because of the larger diameter of the Na-ion (0.97 Å) compared to Li-ion (0.68 Å), it's difficult to develop the suitable host for Na-ion storage [9]. Now, a major challenge in realizing NIBs was the absence of suitable anode (negative) materials [7]. Hard carbon and some graphite as anode materials for NIBs were reported, however, they presented limited capacity at a high current rate [10,11]. Our study and other group's research found that $TiO_2$ nanostructures displayed a stable cycling stability for Na-ion storage, but it's theoretical capacity is not high enough (ca. 170 mA h $g^{-1}$) [12–14]. Recently, some alloying (Sn and $SnO_2$) [15,16] and conversion reactions (CuO and $MoS_2$) [17,18] anode materials were studied, which exhibited a high initial capacity. However, many of them suffered from poor cycling performance due to the large volume change. In particular, a class of spinel $AB_2O_4$ materials, for example, $Co_3O_4$ nanostructures were used as promising anode material for NIBs owing to its high theoretical capacity of 890 mA h $g^{-1}$ [19,20]. However, because of toxic nature of cobalt and the volume change among the batteries charge and discharge, $Co_3O_4$ has not been considered as an alternative anode material for large-scale manufacture [21].

Ternary metal oxide, $NiCo_2O_4$, has been reported that it has more advantages in promoting the electrochemical performance than those of binary nickel oxides and cobalt oxides [22–25].

* Corresponding author.
** Corresponding author.
*E-mail addresses:* winter0514@fzu.edu.cn (Z. Hong), zghuang@fjnu.edu.cn (Z. Huang).

http://dx.doi.org/10.1016/j.jallcom.2015.08.130
0925-8388/© 2015 Published by Elsevier B.V.

Nevertheless, the Na-ion storage performance of $NiCo_2O_4$ was relatively rare investigated [26–28]. Recently, it's demonstrated that $NiCo_2O_4$ with two-dimensional nanosheets morphology exhibited superior lithium storage performance [21,29,30]. However, the Na-ion storage properties of $NiCo_2O_4$ nanosheets have never been reported. In this study, ultrathin $NiCo_2O_4$ nanosheets with mesoporous structure and a large surface area were fabricated by a facile method. When evaluated as anode material for sodium ion batteries, the ultrathin $NiCo_2O_4$ nanosheets exhibited a high reversible capacity of 690.4 mA h $g^{-1}$ at 100 $mAg^{-1}$ and good rate performance in the voltage window of 0.01–2.5 V.

## 2. Experimental section

### 2.1. Materials synthesis

Two kinds of porous $NiCo_2O_4$ nanosheets with different microstructures, including ultrathin $NiCo_2O_4$ nanosheets ($NiCo_2O_4$-UNSs) and common $NiCo_2O_4$ nanosheets ($NiCo_2O_4$-NSs) were prepared by a facile method under different reaction temperature. Synthesis of ultrathin $NiCo_2O_4$ nanosheets ($NiCo_2O_4$-UNSs): 1 mmol of $Ni(NO_3)_2{\cdot}6H_2O$, 2 mmol of $Co(NO_3)_2{\cdot}6H_2O$ and 4.5 mmol of hexamethylenetetramine are dissolved in the solution, consisting of 20 mL ethanol and 40 mL deionized (DI) water, then transferred into 100 mL Teflon-lined. After that, the solution was stirred at 90 °C for one day under magnetic stirrer. After cooling to room temperature, the precipitates were collected by centrifugation and washed with DI water and ethanol for several times. The product was then dried in the blast oven at 60 °C for 12 h. Finally, the product was annealed at 350 °C for 2 h in air in order to obtain $NiCo_2O_4$-UNSs. Synthesis of $NiCo_2O_4$ nanosheets ($NiCo_2O_4$-NSs): the synthesis process was similar to that of $NiCo_2O_4$-UNSs besides that it was putted into stainless steel autoclave and heated at 150 °C for two days in the blast oven.

### 2.2. Characterizations of the samples

Scanning electron microscopy (SEM, SU8000 instrument) and Transmission electron microscopy (TEM, FEI F20 S-TWIN instrument) were applied for the structural characterization of the resulting nanosheets. X-ray diffraction (XRD) patterns were recorded on a PANalytical X'Pert spectrometer using the Co Kα radiation (λ = 1.78897 Å), and the data were changed to Cu Kα data. $N_2$ adsorption–desorption analysis was measured on a Micro-meritics Tristar II 3020 instrument (USA). The pore size distributions of the as-prepared samples were analyzed using the Barrett Joyner Halenda (BJH) method.

### 2.3. Electrochemical measurements

For the electrochemical measurement of sodium half-cells, both of mesoporous $NiCo_2O_4$ nanosheets were admixed with acetylene black carbon and polyvinylidene fluoride (PVDF) binder in a weigh ratio of 70:20:10. The mixtures were spread and pressed on copper foil circular flakes as working electrodes (WE), and dried at 120 °C in vacuum for 12 h. Sodium ion batteries were assembled in coin-type cells (CR 2025) with a Na metal foil as the counter electrode, glass fiber separator (Whatman GF/F), and 1 M $NaClO_4$ in ethylene carbonate (EC) and diethyl carbonate (DEC) (1/1 in volume) as the electrolyte. The cells were assembled in a glove box filled with highly pure argon gas ($O_2$ and $H_2O$ levels < 1 ppm), and charge/discharge tests were performed in the voltage range of 0.01–2.5 V ($Na^+$/Na) on a Land automatic batteries tester (Land CT 2001A, Wuhan, China). Cyclic voltammetry (CV) measurements were performed on Zennium (Zahner).

## 3. Results and discussion

Two kinds of the $NiCo_2O_4$ nanosheets with different microstructures, including ultrathin $NiCo_2O_4$ nanosheets ($NiCo_2O_4$-UNSs) and common $NiCo_2O_4$ nanosheets ($NiCo_2O_4$-NSs), were synthesized under different reaction temperature. The crystalline structure and phase purity of the $NiCo_2O_4$ materials were characterized by XRD. Fig. 1 shows the XRD patterns of the $NiCo_2O_4$ nanosheets. Eight distinct diffraction peaks are observed at 2$\theta$ values of 19.3°, 31.2°, 36.8°, 38.5°, 44.8°, 55.8°, 59.3°, and 65.2° can be indexed to the (111), (220), (311), (222), (400), (422), (511), and (440) crystal planes of $NiCo_2O_4$ (JCPDS No. 20-0781), respectively. Moreover, no other impurity peaks were observed from the XRD patterns, which revealed that both of the two samples were pure spinel $NiCo_2O_4$. It could be observed from Fig. 1 that $NiCo_2O_4$-UNSs prepared under 90 °C exhibited much broader diffraction peaks than that of $NiCo_2O_4$-NSs prepared under 150 °C, indicating the smaller crystallite size of this material. In addition, the average sizes of $NiCo_2O_4$-UNSs and $NiCo_2O_4$-NSs were calculated to be ca. 10 nm and ca. 13 nm, respectively, using the Scherer equation based on (311) diffraction peak from Fig. 1.

The low-magnification and high-magnification scanning electron microscopy (SEM) images of the $NiCo_2O_4$-UNSs were depicted in Fig. 2a and Fig. 2b. It's shown clearly that the numerous nanosheets interconnected with each other were formed. The porous nature of nanosheets could be observed for the high-magnification SEM image (Fig. 2b). From a top view SEM image (inset of Fig. 2b), it could be revealed that the thickness of the ultrathin nanosheets was found to be less than 10 nm. The transmission electron microscope (TEM) images were used to further characterize the microstructure of the nanosheets, as shown in Fig. 2c and d. It could be clearly observed that $NiCo_2O_4$-UNSs are constructed by $NiCo_2O_4$ nanoparticle subunits interconnected to each other, leading to the formation of a large number of interparticle pores. Such porous nanostructures could provide extra space to store more sodium ions and high level of contact between the electrode and electrolyte. Fig. 2d shows the HRTEM image of $NiCo_2O_4$-UNSs, which obviously reveals the clear lattice fringes of ca. 0.25 nm, corresponding to the (311) crystal plane of spinel $NiCo_2O_4$. In order to compare with the $NiCo_2O_4$-UNSs, the SEM and TEM images of $NiCo_2O_4$-NSs are shown in Fig. 3. $NiCo_2O_4$-NSs synthesized under 150 °C also have a nanosheet morphology with porous structure, as depicted in Fig. 3a and b. However, such nanosheets display a larger thickness (about 20 nm) than that of $NiCo_2O_4$-UNSs. Meanwhile, TEM image (Fig. 3c) further revealed that the nanosheets were composed of nanoparticle subunits. The porous nature could be further opened up from the HRTEM image (Fig. 3d), and the clear lattice fringes of the (220) crystal plane for the $NiCo_2O_4$-NSs with a spacing of ca. 0.29 nm can be also observed. Herein, the results

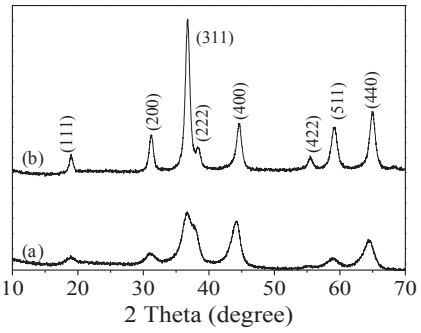


**Fig. 1.** XRD patterns of the $NiCo_2O_4$-UNSs and the $NiCo_2O_4$-NSs synthesized at 90 °C (a) and 150 °C (b).

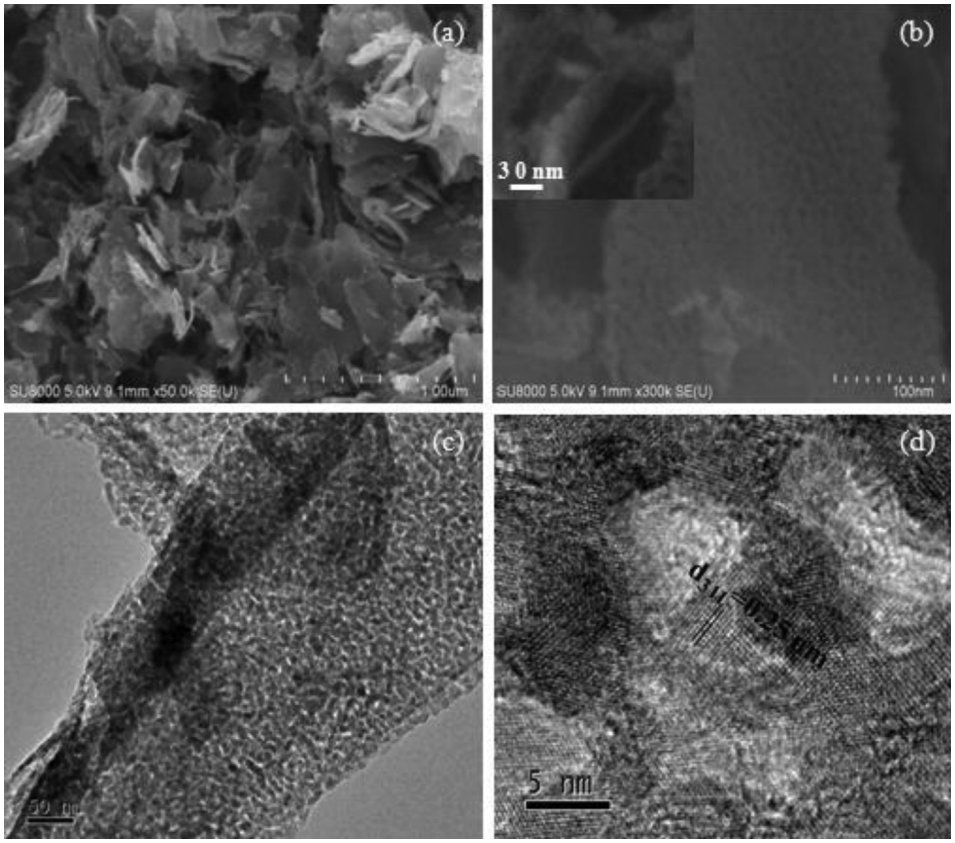


**Fig. 2.** SEM (a–b), TEM (c) and HRTEM (d) images of the $NiCo_2O_4$-UNSs. The inset in (b) is a high magnification SEM image.

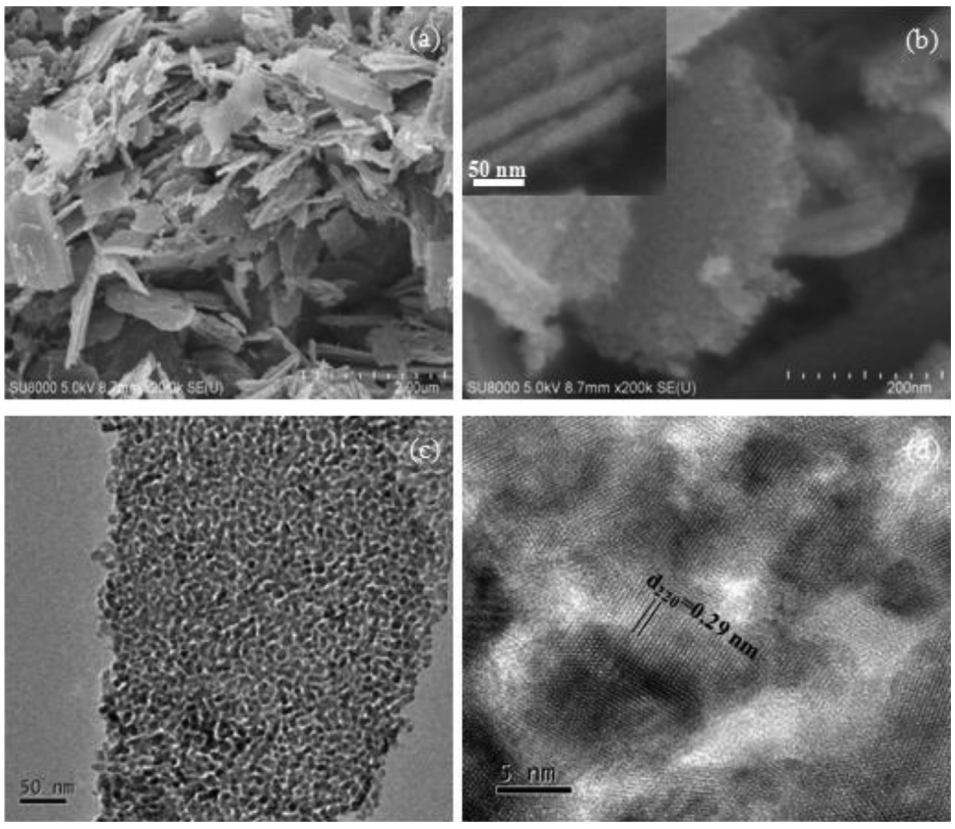


**Fig. 3.** SEM (a–b), TEM (c) and HRTEM (d) images of the $NiCo_2O_4$-NSs. The inset (b) is a high magnification SEM image.

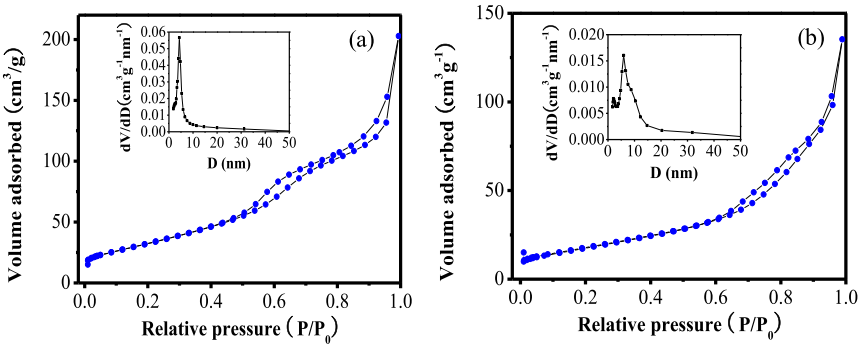


**Fig. 4.** Nitrogen adsorption/desorption isotherms and BJH pore size distributions (inset) of the $NiCo_2O_4$-UNSs (a) and the $NiCo_2O_4$-NSs (b).

demonstrate that the porous $NiCo_2O_4$ nanosheets with different thickness were successfully prepared.

To confirm the porous nature of the $NiCo_2O_4$ nanosheets, the nitrogen adsorption–desorption isotherms were measured, as presented in Fig. 4. Both of the isotherms in Fig. 4a and b can be categorized as same type of isotherm (type IV) with H1 hysteresis loop, which indicates a characteristic mesoporous structure. As shown in the insets of Fig. 4a and b, the mesoporous structure of the $NiCo_2O_4$ UNSs and NSs are further confirmed by the Barrett–Joyner–Halenda (BJH) pore size distribution data. It is worth mentioning that the pore size distribution of the $NiCo_2O_4$-UNSs is relatively narrow with most of the pore size around 5 nm, but the pore distribution of the $NiCo_2O_4$-NSs is evenly distributed in the range of 5–10 nm. Thus, it's suggested that the pore size distribution of the $NiCo_2O_4$-UNSs is more uniform than the $NiCo_2O_4$-NSs. In addition, the Brunauer–Emmett–Teller (BET) surface area and pore

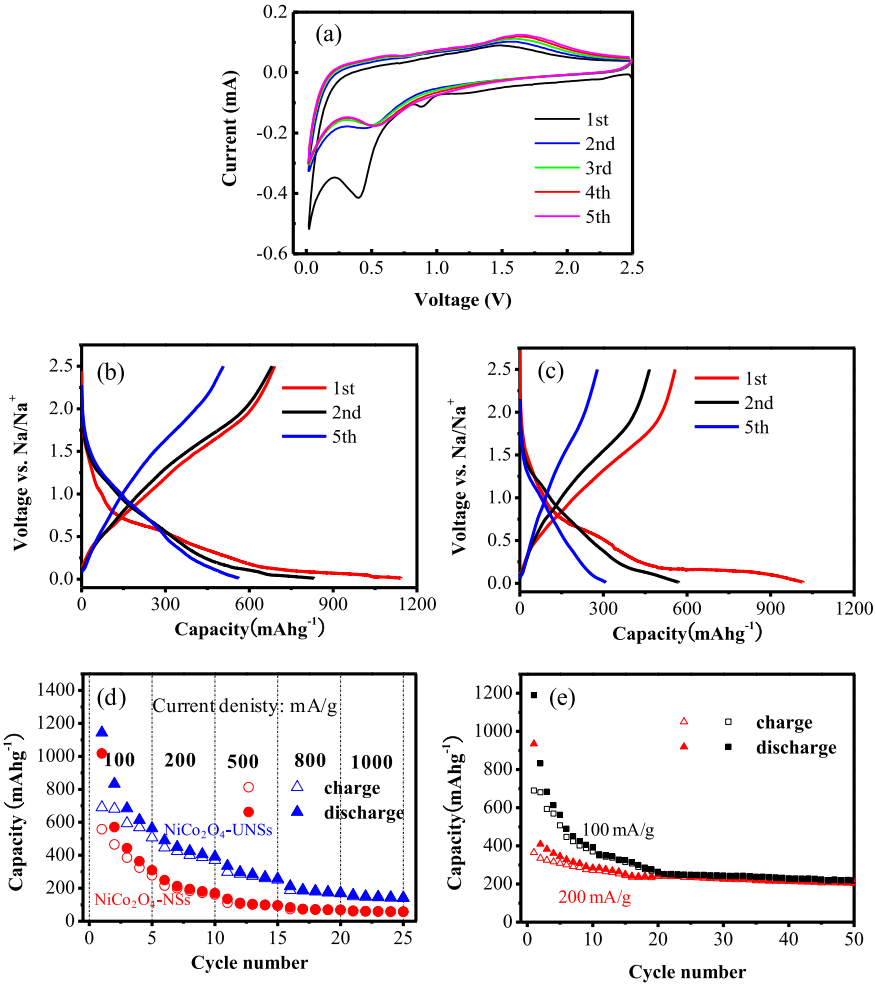


**Fig. 5.** (a) First five consecutive CV curves of the $NiCo_2O_4$-UNSs at a scan rate of 0.5 mV/s, galvanostatic discharge and charge profiles at the 1st, 2nd and 5th cycle of $NiCo_2O_4$-UNSs (b) and $NiCo_2O_4$-NSs (c), (d) rate performance for the $NiCo_2O_4$-UNSs (blue) and the $NiCo_2O_4$-NSs (red) at the current densities from 100 to 1000 mA/g, (e) cycling performance of the $NiCo_2O_4$-UNSs electrode at a current density of 100 and 200 mA/g. (For interpretation of the references to color in this figure legend, the reader is referred to the web version of this article).

volume of the $NiCo_2O_4$-UNSs are 119 $m^2\ g^{-1}$ (67 $m^2\ g^{-1}$ for $NiCo_2O_4$-NSs) and 0.31 $cm^3\ g^{-1}$ (0.21 $cm^3\ g^{-1}$ for $NiCo_2O_4$-NSs), respectively. Because the more outstanding mesoporous feature and larger surface area facilitate the $Na^+$ ion diffusion and intercalation as well as well contacts between electrode-electrolyte, it's expected that the $NiCo_2O_4$-UNSs could present more excellent electrochemical performance than the $NiCo_2O_4$-NSs.

In order to test the electrochemical performance of the UNSs, the cyclic voltammetry (CV) was conducted. Fig. 5a shows the first five CV curves of the $NiCo_2O_4$ UNSs in the potential window of 0.01–2.5 V. In the first cycle of the $NiCo_2O_4$ UNSs, as shown in Fig. 5a, the intense cathodic peak located at 0.4 V may result from the reduction of mixed oxide to metallic Co and Ni, respectively. The anodic peak is observed at 1.5 V, which could be attributed to the oxidation of metallic Ni and Co to nickel oxides and cobalt oxides. In the next four cycles, the redox peaks around 0.6 V and 1.6 V correspond to the reduction and oxidation of the nickel oxides and cobalt oxides [24,31]. This result is corresponding to the previous reports [26–28]. In other words, the Na-ion storage process for $NiCo_2O_4$ electrode is similar to that of Li-ion.

Fig. 5b and c show the charge–discharge profiles of the $NiCo_2O_4$-UNSs and $NiCo_2O_4$-NSs electrodes at a current density of 100 mA $g^{-1}$ in the potential window of 0.01–2.5 V, respectively. In the first discharge process, both of the electrodes exhibit a potential plateau around 0.2 V, which may be due to the phase decompose of the spinel structure. Similar results were also found for $Co_3O_4$ anode for Na-ion storage [31]. In Fig. 5b, the first discharge capacity of the $NiCo_2O_4$-UNSs can reach 1143.5 mA h $g^{-1}$ and the consequent charge capacity can reach 690.4 mA h $g^{-1}$. Meanwhile, the capacity reduced gradually with the increase of the cycle number, the discharge and charge capacity were reduced to 563 mA h $g^{-1}$ and 507.2 mA h $g^{-1}$ at the fifth cycle. As for $NiCo_2O_4$-NSs (see Fig. 5c), the first discharge capacity of the NSs is 1017.1 mA h $g^{-1}$ and the consequent charge capacity is 557.4 mA h $g^{-1}$. Similarly, the discharge–charge capacity also reduced to 308.9 mA h $g^{-1}$ and 278.2 mA h $g^{-1}$ at the fifth cycle. Thus, the initial coulombic efficiency of the $NiCo_2O_4$ UNSs and NSs are a little low, but it was remarkably improved after five cycles, close to 100%. This may be due to the irreversible reaction for the electrode material and solid electrolyte interface (SEI) formed on the surface of the electrode at the first cycle [27,28]. It could be also obtained that the capacity of the $NiCo_2O_4$-UNSs decayed more slowly than that of $NiCo_2O_4$-NSs. Next, the current rate capability of the UNSs and NSs were measured, respectively. As shown in Fig. 5d, $NiCo_2O_4$-UNSs exhibit much better rate capability than that of $NiCo_2O_4$-NSs at different current densities ranging from 100 to 1000 mA $g^{-1}$. At the current density of 1000 mA $g^{-1}$, the $NiCo_2O_4$-UNSs still delivers a reversible capacity of 141.8 mA h $g^{-1}$, while the capacity of $NiCo_2O_4$-NSs was only 57.2 mA h $g^{-1}$ at the same condition. The enhanced sodium-ion storage performance of $NiCo_2O_4$-UNSs could be largely due to the larger surface and more outstanding mesoporous feature, which provide much more active sites and a better accessibility for the electrolyte, leading to a high reversible capacity and improved rate capability. Fig. 5e presents the cycling performance of the $NiCo_2O_4$-UNSs at a constant current rate of 200 mA $g^{-1}$. Before 20 cycles, the capacity of the UNSs reduces relatively quickly, but the capacity tended to keep relatively stability after the consequent cycles. Furthermore, a reversible capacity of about 207.1 and 203.7 mA h $g^{-1}$ can be remained after 50 cycles at 100 and 200 $mAg^{-1}$, respectively.

## 4. Conclusions

In conclusion, two kinds of the $NiCo_2O_4$ nanosheets ($NiCo_2O_4$-UNSs and $NiCo_2O_4$-NSs) composed of interconnected nanoparticles with different microstructures were controllably synthesized by a facile method. $NiCo_2O_4$-UNSs with ultrathin thickness have a mesoporous structure, large surface area (119 $m^2\ g^{-1}$) and narrow pore distribution (around 5 nm). Then, these $NiCo_2O_4$ nanosheets were used for the first time as the anode materials for NIBs. $NiCo_2O_4$-UNSs exhibited a high reversible capacity of 690.4 mA h $g^{-1}$ at 100 $mAg^{-1}$ in the voltage window of 0.01–2.5 V and good rate performance. The enhanced sodium-ion storage performance of $NiCo_2O_4$-UNSs could be largely due to the larger surface and more outstanding mesoporous feature, which provide more active sites and a good accessibility for the electrolyte, leading to a high reversible capacity and better rate capability.

## Acknowledgments

This work was financially supported by National Natural Science Foundation of China (NSFC 21205016), National Science Foundation of Fujian Province (2015J01042), Education Department of Fujian Province (JA14081, JB13008).

## References

[1] J.M. Tarascon, M. Armand, Nature 414 (2001) 359–367.
[2] J.B. Goodenough, Y. Kim, Chem. Mater. 22 (2010) 587–603.
[3] J.-M. Tarascon, Nat. Chem. 2 (2010) 510.
[4] B.L. Ellis, W.R.M. Makahnouk, Y. Makimura, K. Toghill, L.F. Nazar, Nat. Mater. 6 (2007) 749–753.
[5] H. Pan, Y.-S. Hu, L. Chen, Energy Environ. Sci. 6 (2013) 2338–2360.
[6] N. Yabuuchi, K. Kubota, M. Dahbi, S. Komaba, Chem. Rev. 114 (2014) 11636–11682.
[7] Y. Kim, K.-H. Ha, S.M. Oh, K.T. Lee, Chem.-Eur. J. 20 (2014) 11980–11992.
[8] M.M. Doeff, Y. Ma, S.J. Visco, L.C. De Jonghe, J. Electrochem. Soc. 140 (1993) L169–L170.
[9] D.A. Stevens, J.R. Dahn, J. Electrochem. Soc. 148 (2001) A803–A811.
[10] K. Tang, L. Fu, R.J. White, L. Yu, M.-M. Titirici, M. Antonietti, J. Maier, Adv. Energy Mater. 2 (2012) 873–877.
[11] A. Ponrouch, A.R. Goñi, M.R. Palacín, Electrochem. Commun. 27 (2013) 85–88.
[12] Z. Hong, K. Zhou, Z. Huang, M. Wei, Sci. Rep. 5 (2015) 11960.
[13] K.T. Kim, G. Ali, K.Y. Chung, C.S. Yoon, H. Yashiro, Y.-K. Sun, J. Lu, K. Amine, S.-T. Myung, Nano Lett. 14 (2014) 416–422.
[14] X. Yang, C. Wang, Y. Yang, Y. Zhang, X. Jia, J. Chen, X. Ji, J. Mater. Chem. A 3 (2015) 8800–8807.
[15] Y. Xu, Y. Zhu, Y. Liu, C. Wang, Adv. Energy Mater. 3 (2013) 128–133.
[16] Y. Liu, Y. Xu, Y. Zhu, J.N. Culver, C.A. Lundgren, K. Xu, C. Wang, ACS Nano 7 (2013) 3627–3634.
[17] L. Wang, K. Zhang, Z. Hu, W. Duan, F. Cheng, J. Chen, Nano Res. 7 (2014) 199–208.
[18] C. Zhu, X. Mu, P.A. van Aken, Y. Yu, J. Maier, Angew. Chem. Int. Ed. 53 (2014) 2152–2156.
[19] Z. Jian, P. Liu, F. Li, M. Chen, H. Zhou, J. Mater. Chem. A 2 (2014) 13805–13809.
[20] K.C. Klavetter, S. Garcia, N. Dahal, J.L. Snider, J. Pedro de Souza, T.H. Cell, M.A. Cassara, A. Heller, S.M. Humphrey, C.B. Mullins, J. Mater. Chem. A 2 (2014) 14209–14221.
[21] A.K. Mondal, D. Su, S. Chen, X. Xie, G. Wang, ACS Appl. Mater. Interfaces 6 (2014) 14827–14835.
[22] H. Shi, G. Zhao, J. Phys. Chem. C 118 (2014) 25939–25946.
[23] J. Zhang, Q. Lu, J. Fang, J. Wang, J. Yang, Y. NuLi, ACS Appl. Mater. Interfaces 6 (2014) 17965–17973.
[24] X.-Y. Yu, X.-Z. Yao, T. Luo, Y. Jia, J.-H. Liu, X.-J. Huang, ACS Appl. Mater. Interfaces 6 (2014) 3689–3695.
[25] G. Zhang, X.W. Lou, Sci. Rep. 3 (2013) 1470.
[26] R. Alcántara, M. Jaraba, P. Lavela, J.L. Tirado, Chem. Mater. 14 (2002) 2847–2848.
[27] A. Thissen, D. Ensling, F.J. Fernández Madrigal, W. Jaegermann, R. Alcántara, P. Lavela, J.L. Tirado, Chem. Mater. 17 (2005) 5202–5208.
[28] A.V. Chadwick, S.L.P. Savin, S. Fiddy, R. Alcantara, D.F. Lisbona, P. Lavela, G.F. Ortiz, J.L. Tirado, J. Phys. Chem. C 111 (2007) 4636–4642.
[29] I. Shakir, M. Sarfraz, U.A. Rana, M. Nadeem, M.A. Al-Shaikha, RSC Adv. 3 (2013) 21386–21389.
[30] L. Zhang, S. Zhang, K. Zhang, G. Xu, X. He, S. Dong, Z. Liu, C. Huang, L. Gu, G. Cui, Chem. Commun. 49 (2013) 3540–3542.
[31] M.M. Rahman, A.M. Glushenkov, T. Ramireddy, Y. Chen, Chem. Commun. 50 (2014) 5057–5060.